MDPI

Article

Effect of Nitrogen Doping on the Structure and Mechanical Properties of the $Fe_{40}Mn_{40}Cr_{10}Co_{10}$ High-Entropy Alloy

Anastasiia Semenyuk [1,*], Elizaveta Povolyaeva [1], Vitalii Sanin [2], Sergey Zherebtsov [1] and Nikita Stepanov [1]

[1] Laboratory of Bulk Nanostructured Materials, Belgorod State University, 308015 Belgorod, Russia
[2] Laboratory of Thermomechanical Processes, National University of Science and Technology MISiS, 119049 Moscow, Russia
* Correspondence: semenyuk@bsu.edu.ru

Abstract: The structure and mechanical properties of as-cast and thermomechanicaly processed (cold rolling followed by annealing at 700 °C and 900 °C) $Fe_{40}Mn_{40}Cr_{10}Co_{10}$ (at.%) high-entropy alloys doped with different amounts (0, 0.5, and 2.0 at.%) of N were examined. The as-cast $Fe_{40}Mn_{40}Cr_{10}Co_{10}$ alloy (N0) contained σ-phase particles at the boundaries of the fcc grains. The addition of 0.5 (N0.5) and 2.0 (N2) at.% of nitrogen suppressed the formation of the σ-phase due to which the alloys consisted of only the fcc phase. Annealing after rolling resulted in the development of static recrystallization and precipitation of additional phases: the σ-phase was found in the N0 and N0.5 alloys, and hexagonal M_2N nitrides were found in the N2 alloy. The strength of the as-cast alloys at room temperature increased with increasing nitrogen concentration due to interstitial solid solution strengthening. Cold rolling and subsequent annealing resulted in considerable strengthening of the program alloys. The strength of the alloys increased with the N content and decreased with increasing annealing temperature. The best combination of mechanical properties at room temperature was attained in the N2 alloy after annealing at 700 °C, and at 77 K, was demonstrated by the N0.5 alloy after annealing at 900 °C.

Keywords: high-entropy alloys; nitrogen; σ-phase; thermomechanical processing; mechanical properties

1. Introduction

The so-called high entropy alloys (HEAs) are multicomponent (usually, ≥ 5) alloys in which constitutive elements occur in roughly equal atomic fractions [1,2]. Due to their unique structures and properties, they are often considered promising materials for industrial, aerospace, and biomedical applications [3,4]. For example, HEAs based on refractory elements are considered to be possible next-generation high-temperature materials beyond Ni-based superalloys [5,6].

In recent years, much attention has been paid to model single-phase alloys with simple crystal structures, such as face-centered cubic (fcc) and body-center cubic (bcc); it is believed that such alloys can have a good strength–ductility combination [7,8]. These alloys also correspond nicely to the original concept of HEAs. For example, alloys of the Co-Cr-Fe-Mn-Ni system tend to form a single fcc solid solution structure and at the same time have promising properties [9]. For instance, equiatomic CoCrFeMnNi and CoCrNi alloys have high ductility and fracture toughness, not only at room temperature, but also at cryogenic temperatures [10–14]. However, one of the recent trends in the HEA design is associated with non-equiatomic concentrations of the constitutive elements. In this case, the composition of the alloy can be flexibly tailored to produce new alloys with desired properties [15–17]. For example, in the $Fe_{80-x}Mn_xCo_{10}Cr_{10}$ alloy family, a stable single fcc phase structure was observed at x = 45 and x = 40, whereas a lower Mn content ($x \leq 35$) resulted in the fcc→hcp martensitic transformation [11]. The non-equiatomic

$Fe_{40}Mn_{40}Co_{10}Cr_{10}$ alloy was considered one of the promising HEAs, with properties similar to equiatomic CoCrFeMnNi and, simultaneously, with a significantly reduced cost due to a lower content of expensive Co and Ni [18].

However, the formation of a single-phase solid solution structure is observed quite rarely. A variety of different intermetallic phases can be found in HEAs depending on the alloy composition and the processing conditions [19–23]. For example, in Co-Cr-Fe-Mn-Ni-based alloys, the formation of a chromium-rich σ-phase with a tetragonal structure is often described [24–27]. Earlier, the σ-phase was frequently found in different steels [28] and nickel superalloys [29]. However, the σ-phase is intrinsically brittle and is usually considered an undesirable phase since the presence of the σ-phase results in significant embrittlement of the material [30]. Although in some cases the σ-phase formation provided considerable hardening without noticeable loss in ductility due to the extremely high strain-hardening capacity of the fcc matrix (for example, in a $CoCrFeNiMo_{0.3}$ alloy [31]), an increase in the fraction of the σ-phase usually results in a serious loss in ductility of the material [12,22]. In addition, partitioning of Cr from the fcc matrix to the σ-phase can deteriorate both the oxidation resistance [32] and strength, as Cr is a strong solid-solution hardener in fcc HEAs [33]. It is worth noting that the σ-phase inhibits grain growth, thus effectively strengthening the material [24,27]. In the $Fe_{40}Mn_{40}Co_{10}Cr_{10}$ alloy, the σ-phase is reported to appear after heat treatment at $\leq 700\ °C$ [22,23].

The common approach to improve the performance of the fcc HEAs is associated with the doping with interstitial elements such as carbon or nitrogen. Interstitials can have multifaceted effects on the structure and performance of the alloys, including the (i) solid solution strengthening effect [34,35]; (ii) activation of the additional deformation mechanisms such as TWIP/MBIP [36–40]; precipitation hardening by carbides/nitrides after proper heat treatment and/or thermomechanical processing [41,42]; refinement of the fcc grains due to the carbide/nitride pinning effect [43,44]. As a result, simultaneous improvement of strength and ductility can be achieved [34,39,44]. Recent efforts demonstrate that alloying with nitrogen strengthens alloys more pronouncedly in comparison with other interstitial elements [35,36,41–45]. However, the information on the interstitial doping of the $Fe_{40}Mn_{40}Co_{10}Cr_{10}$ alloy is limited; a positive effect of a small amount of boron addition on the strength–ductility combination was revealed in [46]. The effect was associated with boron segregation to the fcc grain boundaries and limiting their mobility, thus producing a fine-grained structure [35–37].

In this work, we examined the structure of the $Fe_{40}Mn_{40}Co_{10}Cr_{10}$ alloy doped with different amounts of N (0–2 at.%) after thermomechanical processing. The amounts of added nitrogen were selected based on a literature analysis [34,37,44,47–49]. The final goal was to establish compositions and processing routes ensuring optimal mechanical performance at room and cryogenic temperatures. In addition, specific attention was paid to the interaction between the nitrogen alloying and possible σ-phase precipitation, which is a novel point in HEA research. We hope that the preformed research will benefit the development of cost-effective interstitial HEAs with properties suitable for cryogenic applications.

2. Materials and Methods

High-entropy alloys with the nominal composition of $Fe_{40-x}Mn_{40}Co_{10}Cr_{10}N_x$ (x = 0, 0.5, 2.0) were fabricated by vacuum induction melting. Hereafter, the alloys will be designated according to the nominal nitrogen content, i.e., N0, N0.5, N2. The ingots were cast using mixtures of pure ($\geq$99.9% wt.%) constitutive chemical elements. N was added in the form of ferrochrome nitride. The produced ingots of ~4 kg had a rectangular shape that measured $150 \times 115 \times 35\ mm^3$. The actual chemical composition (measured by energy-dispersive spectrometry (metallic elements) and inert gas fusion (nitrogen)) and density (by Archimedes method) of the alloys is provided in Table 1.

Table 1. Measured chemical composition of the program alloys.

Composition	Density (g/sm^3)	Fe	Mn	Co	Cr	N
		N0				
Nominal (at.%)	7.72	40	40	10	10	-
Actual (at.%)		40.10	40.02	10.03	9.85	-
		N0.5				
Nominal (at.%)	7.67	39.5	40	10	10	0.5
Actual (at.%)		39.55	40.14	9.97	9.9	0.44
		N2.0				
Nominal (at.%)	7.65	38	40	10	10	2
Actual (at.%)		38.5	39.73	10.01	9.94	1.82

Samples with dimensions of $85 \times 35 \times 25$ mm^3 were cut from the as-cast ingots by an electric discharge machine (Sodick, Schaumburg, IL, USA). Unidirectional multipass rolling to a total thickness strain of 80% (from 25 to 5 mm) was performed at room temperature using a thickness reduction per pass of 3–5%. The rolling samples were then annealed in a muffle furnace (Nabertherm, Bahnhofstr, Germany) in air atmosphere at temperatures of 700 °C and 900 °C. The heating time was 10 min followed by air cooling.

The microstructures of the alloy were investigated in the RD-ND plane (perpendicular to the transversal direction). Scanning (SEM), including electron backscattering diffraction (EBSD), and transmission (TEM) electron microscopy were used for the studies. SEM and EBSD studies were carried out using an FEI Quanta 600 FEG microscope (FEI, Hillsboro, OR, USA) equipped with backscattered electron (BSE) and EBSD detectors. Samples for SEM observations were mechanically polished with several SiC papers, and for the finishing polish, we used a colloidal silica suspension. A JEOL JEM-2100 microscope (JEOL, Akishima, Japan) set at an accelerating voltage of 200 kV equipped with an EDS detector was used for TEM investigations. Selected area electron diffraction (SAED) (JEOL, Akishima, Japan) patterns were used for the phase identification and results of EDS for chemical analysis. Samples for TEM analysis were prepared by conventional twin-jet electro-polishing of mechanically pre-thinned to 100 μm foils, in a mixture of 90% CH_3COOH and 10% $HClO_4$, at a 24 V potential at room temperature.

Tensile tests were carried out on an Instron 5882 universal electronic tensile testing machine (Instron, Norwood, MA, USA) at a strain rate of 1×10^{-3} s^{-1} at room (293 K) and cryogenic (77 K) temperatures using samples with a gage that measured $16 \times 3 \times 1.5$ mm^3. For investigation at cryogenic temperature, the test samples and both grips were held in an open-top vessel filled with liquid nitrogen before the test was started to equilibrate the temperature. Elongation to fracture was determined by measuring the spacing between marks designating the gauge length before and after the test. The fracture toughness tests were carried out at room and cryogenic temperatures on an Instron IMP460 pendulum impact machine (Instron, Norwood, MA, USA) using Charpy V-notch specimens that measured $55 \times 8 \times 2$ mm^3. At least 3 specimens per condition were tested.

The equilibrium phase diagrams were constructed using Thermo-Calc software; a TCFE7.0 (steel alloys) database was used since it provides more accurate results for the N-doped alloys in comparison with a specialized database for high-entropy alloys (TCHEA4.0) (Thermo-Calc Software, Solna, Sweden).

3. Results

3.1. Microstructure and Mechanical Properties in the As-Cast Condition

The SEM-BSE images and EBSD phase maps of the as-cast microstructures of the program alloys are shown in Figure 1. A dual-phase microstructure was revealed in the N0 alloy. The second phase particles were found along the grain boundaries of the fcc matrix and inside some grains as thin films (Figure 1c). EBSD analysis and selected area electron diffraction (SAED) patterns allowed us to identify the second phase as the tetragonal

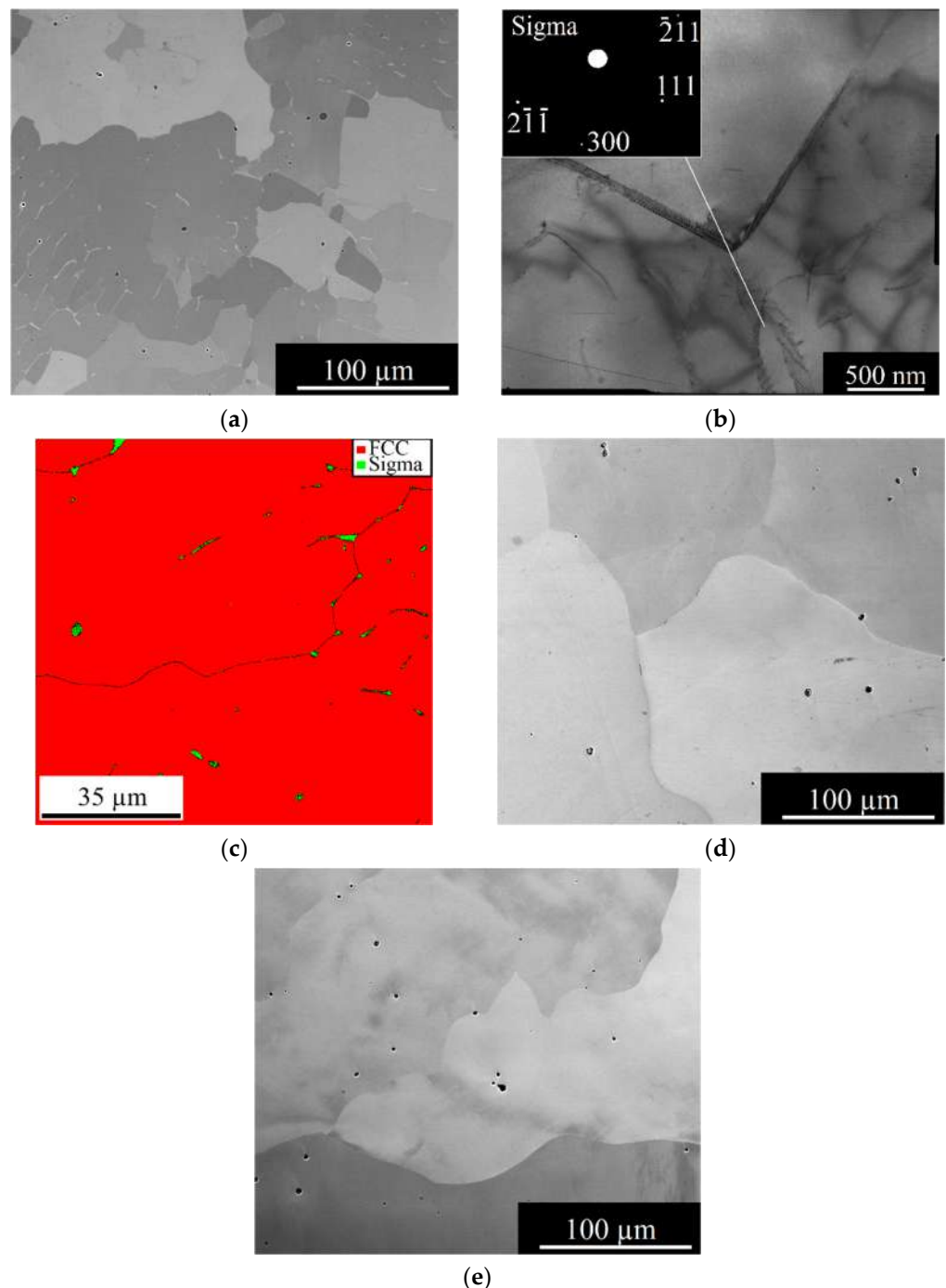σ-phase enriched with Cr, Fe, and Mn; the volume fraction of the σ-phase was 3%. The average fcc grain size was 42 μm.

Figure 1. Microstructure of the $Fe_{40-x}Mn_{40}Cr_{10}Co_{10}N_x$ alloys in the as-cast state: N0 (**a–c**); N0.5 (**d**); N2.0 (**e**); SEM-BSE images (**a,d,e**) TEM image (**b**); EBSD phase map (**c**).

The addition of nitrogen resulted in the disappearance of the σ-phase in the N0.5 and N2 alloys. A single fcc phase structure was found in both alloys. The fcc grain size in the N-doped alloys was considerably larger than that in the N0 alloy and approached ~ 200–300 μm. An increase in the size of the fcc grains may be associated with the absence of the secondary σ-phase in the as-cast N-doped alloys.

To evaluate the mechanical properties of the as-cast alloys, tensile tests at room and cryogenic temperature were performed. The obtained stress–strain curves are presented

in Figure 2, and the resulting mechanical properties (yield strength (YS), ultimate tensile strength (UTS), uniform elongation (UE), and total elongation (TE)) are given in Table 2. Alloying of nitrogen caused a substantial increase in the yield strength (YS) and ultimate tensile strength (UTS) of the program alloys at room temperature. The N0 alloy had a low YS of 160 MPa. High strain-hardening capacity allowed a UTS of 470 MPa. Increasing the nitrogen concentration resulted in significant hardening: the YS and UTS of the N0.5 alloy were 300 MPa and 610 MPa, respectively. The YS of the N2 alloy was 380 MPa, and the UTS was 660 MPa. The effect of the N content on the ductility was more complex. The N0 alloy had high ductility of 71%. The TE first increased to 88% in the N0.5 alloy and then decreased to 61% in the N2 alloy (Table 2). Finally, some "straightening" of the plastic part of the stress–strain curves with an increase in the N content was noted. Similar behavior associated with the formation of the planar dislocation (sub)structure was earlier reported for the carbon-doped fcc HEAs [31,44].
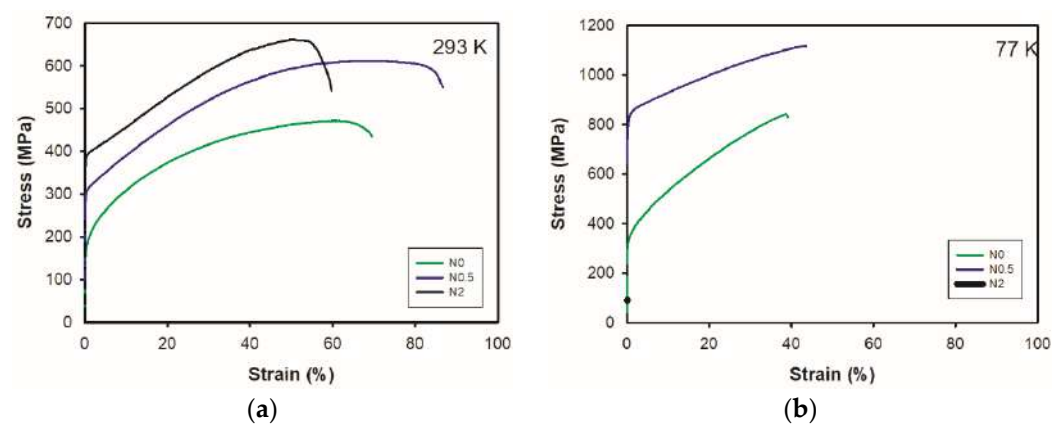

Figure 2. Stress–strain curves of the as-cast $Fe_{40-x}Mn_{40}Cr_{10}Co_{10}N_x$ alloys obtained during tensile testing at room (**a**) and cryogenic (**b**) temperatures.

Table 2. Room and cryogenic temperature mechanical properties of the $Fe_{40-x}Mn_{40}Cr_{10}Co_{10}N_x$ alloys.

Alloy	YS (MPa)	UTS (MPa)	UE (%)	TE (%)
		293 K		
N0	160 ± 20	470 ± 35	63 ± 6	71 ± 9
N0.5	300 ± 25	610 ± 40	70 ± 8	88 ± 9
N2	380 ± 30	660 ± 45	54 ± 5	61 ± 7
		77 K		
N0	320 ± 20	840 ± 40	44 ± 5	44 ± 5
N0.5	800 ± 50	1110 ± 60	45 ± 5	45 ± 4
N2	-	90 ± 10	-	-

The N0 and N0.5 alloys became considerably stronger under cryogenic conditions (Figure 2b). For example, the yield strengths of the N0 and N0.5 alloys were 320 and 800 MPa, respectively, while the ultimate tensile strengths were 840 and 1110 MPa, respectively. The alloys also demonstrated reasonable ductility of 44–45%. The N2 alloy fractured in a brittle manner after reaching a stress of 90 MPa.

3.2. Microstructure after Cold Rolling and Annealing

Cold rolling resulted in the formation of a typical lamellar structure with some shear bands in the program alloys that have been reported for many fcc HEAs [41,44,50]; the representative cold-worked microstructure of the N2 alloy is shown in Figure 3. No noticeable effect of the N content on the microstructure after cold working was detected.
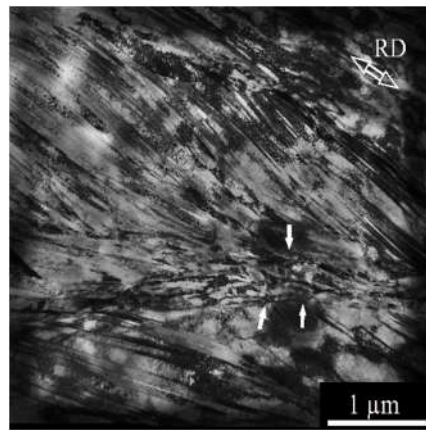
Figure 3. TEM image of the microstructure of the N2 alloy after cold rolling to 80% thickness reduction. The RD arrow indicates the rolling direction.

Further annealing resulted in the development of the static recrystallization and precipitation of additional phases in the $Fe_{40-x}Mn_{40}Cr_{10}Co_{10}N_x$ alloys. The resulting microstructures heavily depended on both the nitrogen content and annealing temperature.

Annealing of the N0 alloy at 700 °C resulted in the formation of a recrystallized structure with a high amount of the σ-phase (Figure 4a,c). The σ-phase particles with a volume fraction of 32% formed a discontinuous network. The σ-phase particles seem to be aligned with the lamellar boundaries and/or shear bands in the cold-rolled alloy. The average recrystallized grain size was 1.3 μm (Table 3). It also seemed that the fcc grains were coarser in the areas free from the σ-phase particles. Increasing the annealing temperature to 900 °C resulted in coarsening of the recrystallized grains to 5.6 μm (Figure 4b,d) while the volume fraction of the σ-phase decreased to 3.6%. The σ-phase precipitated in the form of individual particles arranged in chains. These chains can likely be traced back to the lamellar structure of the deformed condition.

The addition of nitrogen resulted in a decrease in the volume fraction of the σ-phase to 5.2% in the N0.5 alloy after annealing at 700 °C (Figure 5a). The σ-phase particles formed continuous films along grain boundaries. The films were aligned with previous lamellar boundaries and/or shear bands. Recrystallization of the fcc phase appeared to be complete. The average grain size was 2.4 μm. The fcc grains in the vicinity of the σ-particles appeared to be finer than those in the areas free of precipitates. Annealing at a higher temperature of 900 °C resulted in the formation of a homogeneous fully recrystallized single fcc phase structure with the grain size of 6.6 μm (Figure 5b,d). No secondary phases were found.

Table 3. Structural parameters (grain size, fraction, and size of secondary phases) of the $Fe_{40-x}Mn_{40}Cr_{10}Co_{10}N_x$ alloys after annealing at 700 °C and 900 °C.

Alloy	Grain Size (μm)	Particle Size (μm)		Volume Fraction (%)	
		σ-Phase	Nitrides	σ-Phase	Nitrides
Annealing at 700 °C					
N0	1.3	1.3	-	32	-
N0.5	2.4	1.4	-	5.2	-
N2	1.3	-	-	-	7.2
Annealing at 900 °C					
N0	5.6	1.7	-	3.6	-
N0.5	6.6	-	-	-	-
N2	5.8	-	-	-	-
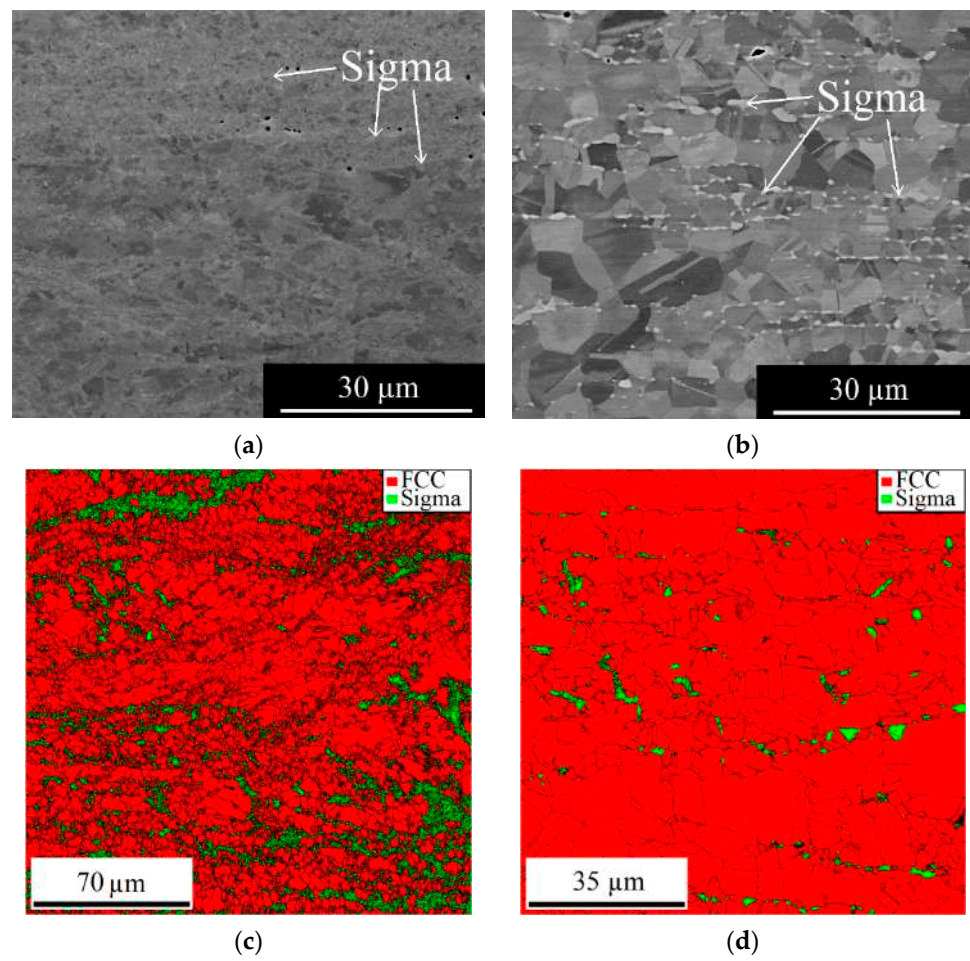
Figure 4. Microstructure of the N0 alloy after cold rolling and annealing at 700 °C (**a**,**c**) and 900 °C (**b**,**d**): SEM-BSE images—(**a**,**b**), EBSD phase maps—(**c**,**d**).
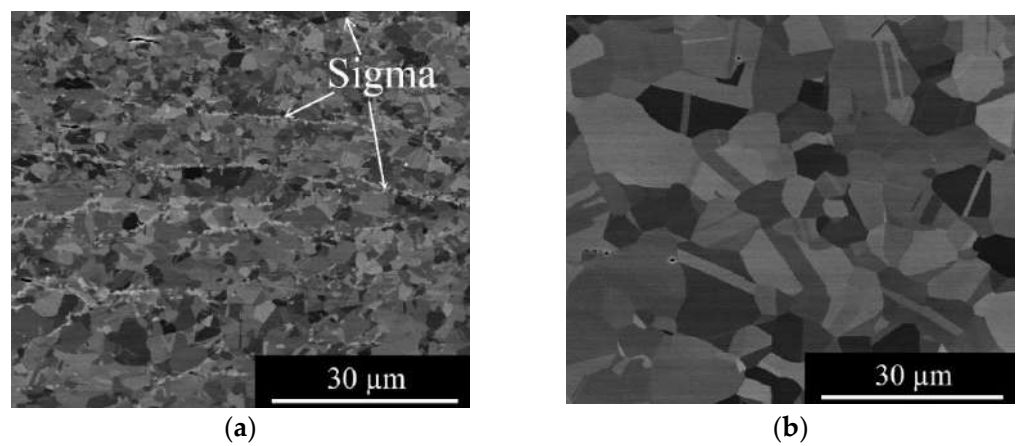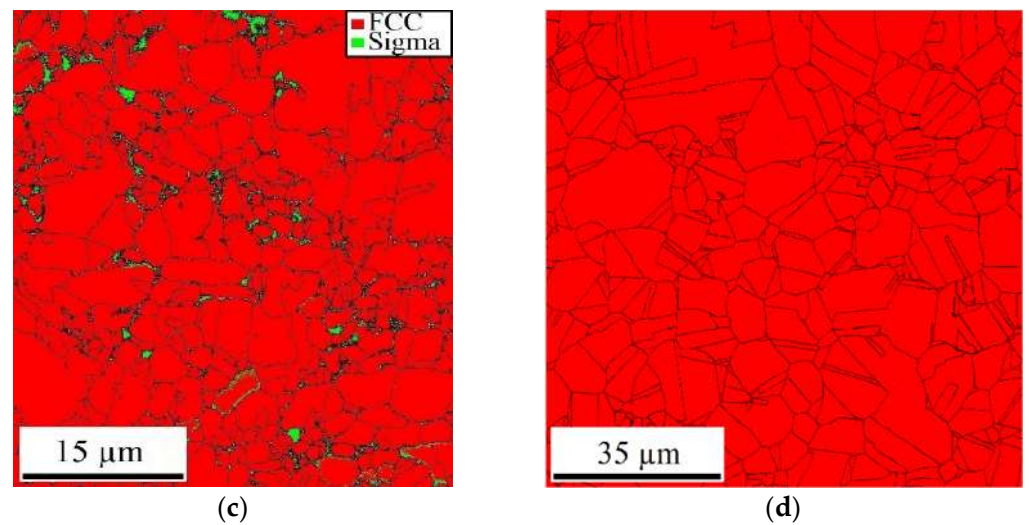

Figure 5. *Cont*.

Figure 5. Microstructure of the N0.5 alloy after cold rolling and annealing at 700 °C (**a**,**c**) and 900 °C (**b**,**d**): SEM-BSE images—(**a**,**b**), EBSD phase maps—(**c**,**d**).

The N2 alloy had a distinctively different microstructure in comparison with the previous alloys. After annealing at 700 °C, only one half (47%) of the microstructure was recrystallized (Figure 6a). The average size of the recrystallized fcc grains was found to be 1.3 μm. More detailed investigations by TEM revealed the presence of fine (~70 nm) Cr-rich precipitates (Figure 6c). Most of these precipitates were found in the recrystallized areas; selected area electron diffraction (SAED) patterns suggested that the particles were hexagonal M_2N nitrides. No signs of the σ-phase particles were found. The increase in the annealing temperature to 900 °C resulted in the formation of a fully recrystallized single fcc phase structure with a grain size of 5.8 μm (Table 3).

3.3. Mechanical Properties

Thermomechanical processing significantly affected the mechanical behavior of the program alloys. Figure 7 shows the tensile stress–strain curves of the alloy obtained during testing at room temperature (Table 4). Apparently, cold rolling with subsequent annealing resulted in considerable strengthening in comparison with the as-cast state. For example, after annealing at 700 °C, the yield strength varied from 650 MPa for the N0 alloy to 900 MPa for the N2 alloy. However, low ductility of the N0 alloy must be noted—the alloy fractures immediately after yielding reached only 1% deformation. The N0.5 and N2 alloys showed respectable ductility of 35–42%. The ultimate tensile strengths of the N0.5 and N2 alloys were 860 MPa and 1100 MPa, respectively.

Table 4. Room temperature mechanical properties of the $Fe_{40-x}Mn_{40}Cr_{10}Co_{10}N_x$ alloys after annealing.

Alloy	YS (MPa)	UTS (MPa)	UE (%)	TE (%)
		Annealing at 700 °C		
N0	650 ± 30	720 ± 40	1 ± 1	1 ± 1
N0.5	620 ± 20	860 ± 45	32 ± 3	47 ± 6
N2	900 ± 35	1100 ± 55	27 ± 4	35 ± 5
		Annealing at 900 °C		
N0	300 ± 20	670 ± 25	40 ± 5	47 ± 7
N0.5	370 ± 20	680 ± 30	47 ± 6	65 ± 9
N2	640 ± 35	940 ± 40	38 ± 5	51 ± 7
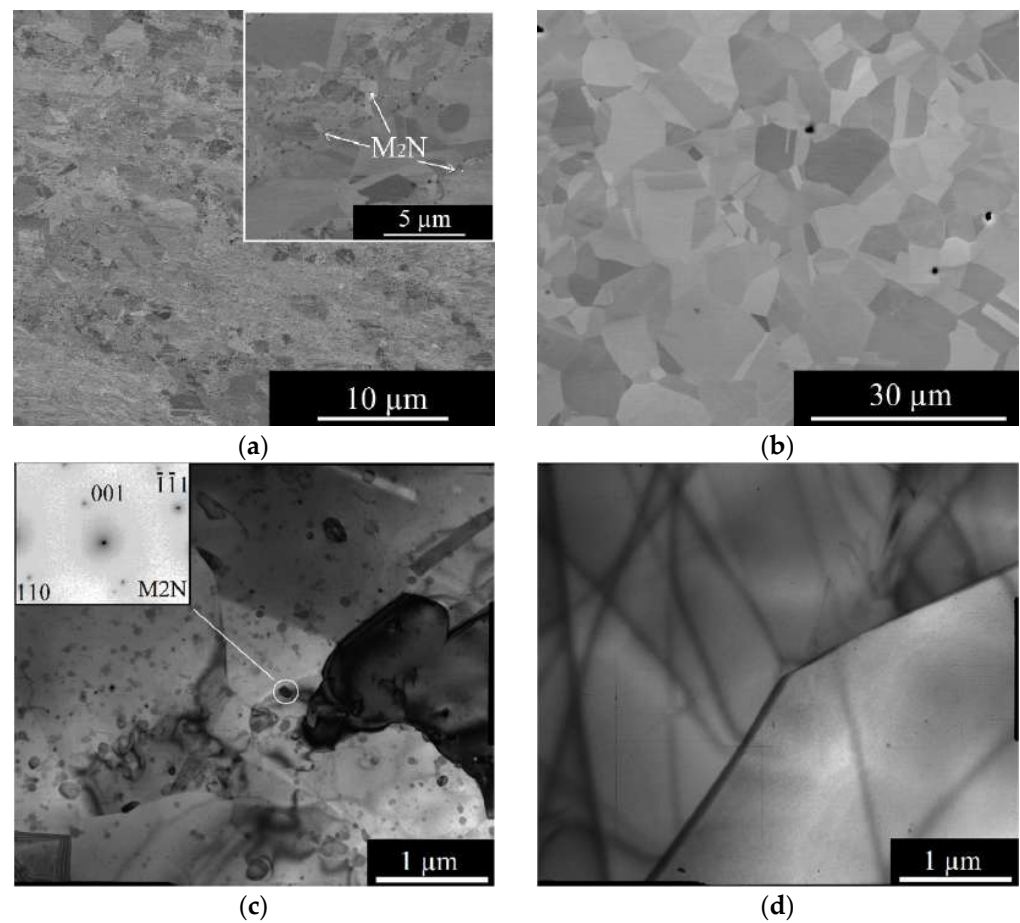
Figure 6. Microstructure of the N2 alloy after cold rolling and annealing at 700 °C (**a**,**c**) and 900 °C (**b**,**d**): SEM-BSE images—(**a**,**b**), EBSD phase maps—(**c**,**d**).
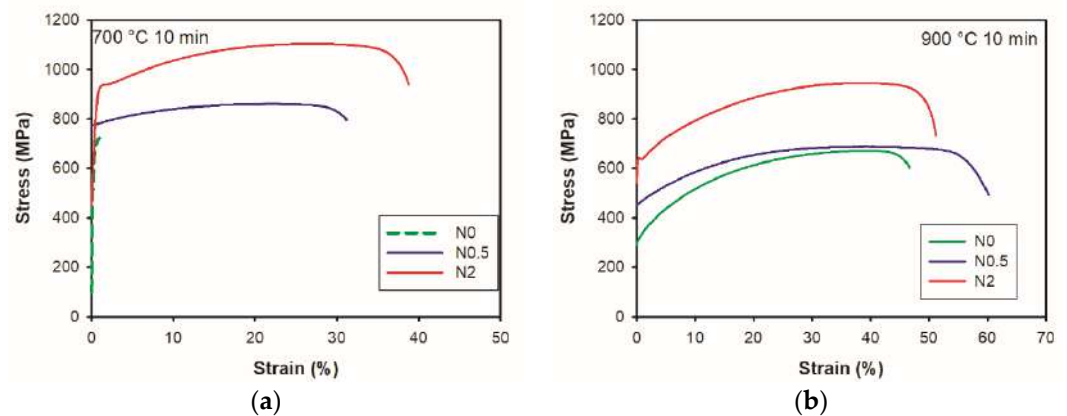

Figure 7. Stress–strain curves of the $Fe_{40-x}Mn_{40}Cr_{10}Co_{10}N_x$ alloys after cold rolling and annealing at 700 °C (**a**) and 900 °C (**b**) obtained during tensile testing at room temperature (293 K).

An increase in the annealing temperature to 900 °C resulted in some decrease in the strength and an increase in the ductility of the alloys. For example, the N0 alloy achieved a total elongation of 47%. The N0.5 alloy showed a much higher ductility of 65%, while the N2 alloy had comparable elongation to fracture (51%). The yield and ultimate tensile strength of the N0 (300 and 670 MPa, respectively) and N0.5 alloy (370 MPa and 680 MPa, respectively) were quite similar, while the N2 alloy was considerably stronger with a yield strength of 640 MPa and an ultimate tensile strength of 940 MPa.

The decrease in the testing temperature to 77 K resulted in drastic changes in the mechanical behavior of the alloys, associated with the strengthening and, most importantly, significant embrittlement (Figure 8, Table 5). For example, after annealing at 700 °C (Figure 8a) only the N0.5 alloy exhibited some ductility (2.5%) while the N0 and N2 alloys fractured during the elastic deformation. Meanwhile, the yield strength of the N0.5 alloy was very high—almost 1500 MPa. After annealing at 900 °C (Figure 8b), the N0 and N0.5 alloys showed reasonable ductility of 56 and 27%, respectively. The yield strength of the alloys was 550 and 1180 MPa, respectively. Meanwhile, the N2 alloy exhibited brittle fracture at the elastic stage.
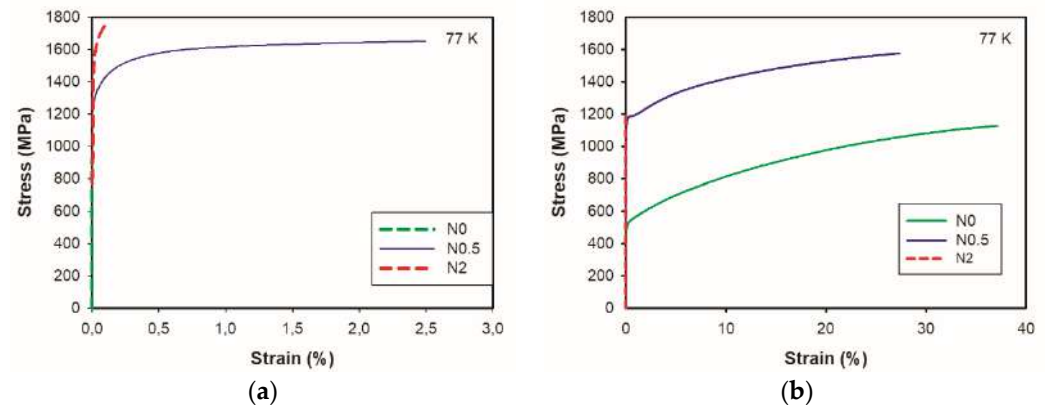

(a)　　　　　　　　　　　　　　　　　　　　　　　　(b)

Figure 8. Stress–strain curves of the $Fe_{40-x}Mn_{40}Cr_{10}Co_{10}N_x$ alloys after cold rolling and annealing at 700 °C (**a**) and 900 °C (**b**) obtained during tensile testing at cryogenic temperature (77 K).

Table 5. The cryogenic mechanical properties of the $Fe_{40-x}Mn_{40}Cr_{10}Co_{10}N_x$ alloys after annealing.

Alloy	YS (MPa)	UTS (MPa)	UE (%)	TE (%)
		Annealing at 700 °C		
N0	-	920 ± 50	-	-
N0.5	1490 ± 70	1650 ± 60	2.5 ± 1	2.5 ± 1
N2	1750 ± 75	1770 ± 70	0.2 ± 0.1	0.2 ± 0.1
		Annealing at 900 °C		
N0	550 ± 20	1230 ± 35	56 ± 8	56 ± 8
N0.5	1180 ± 30	1570 ± 50	27 ± 4	27 ± 5
N2	-	1190 ± 40	-	-

The values of the impact toughness obtained during the Charpy V-notch impact test are summarized in Table 6. The following trends were observed at 293 K: (i) the N0.5 and N2 alloys had considerably higher toughness than the N0 alloy, and (ii) an increase in the annealing temperature resulted in an increase in toughness. In general, all alloys had reasonable toughness at room temperature except for the N0 alloy after annealing at 700 °C (1.6 kJ/m^2). In contrast, at cryogenic temperature, the alloys mostly had low toughness–the only exceptions were the N0 and N0.5 alloys after annealing at 900 °C. The highest toughness was revealed in the N0.5 alloy after annealing at 900 °C–88 and 52 kJ/m^2 at 293 and 77 K, respectively.

Table 6. Impact toughness of the $Fe_{40-x}Mn_{40}Cr_{10}Co_{10}N_x$ alloys after rolling and annealing at 700 °C and 900 °C obtained at room and cryogenic temperatures.

Alloy	Impact Toughness (kJ/m^2)	
	293 K	77 K
Annealing at 700 °C		
N0	1.6 ± 0.5	1.4 ± 0.4
N0.5	21 ± 2	4.0 ± 1.2
N2	23 ± 2	1.3 ± 0.9
Annealing at 900 °C		
N0	35 ± 4	27 ± 4
N0.5	88 ± 8	52 ± 7
N2	74 ± 5	1.2 ± 0.5

4. Discussion

The results obtained revealed that both the microstructure and mechanical properties of the program alloys depended strongly on the chemical composition (N content) and processing conditions. Structure-wise, the most apparent changes were associated with the phase composition. For instance, the N0 alloy in the as-cast state contained a small amount of the σ-phase, while the N0.5 and N2 alloys had a single fcc phase structure (Figure 1). The σ-phase was also found in the N0 alloy after cold working and annealing at 700 and 900 °C (Figure 4), similar to results reported in [22]. At the same time, σ-particles were detected in the N0.5 alloy after annealing at 700 °C, but the same alloy annealed at 900 °C had a single fcc phase. Finally, M_2N nitrides were found in the N2 alloy after annealing at 700 °C. Similar to the N0.5 alloy, the N2 alloy had a single fcc phase structure after annealing at 900 °C.

To rationalize the changes in the observed phases, ThermoCalc software was used to construct the equilibrium $Fe_{40}Mn_{40}Co_{10}Cr_{10}$-N phase diagram (Figure 9). Without regards to N doping, the program alloys are expected to have an fcc phase-based structure, which agrees reasonably with the experimental data. The undoped $Fe_{40}Mn_{40}Co_{10}Cr_{10}$ alloy can also have a small amount of the bcc phase during solidification, as well as the Cr-rich σ-phase at temperatures <712 °C. The addition of N resulted in (i) the suppression of the bcc phase formation; (ii) the gradual decrease in the σ-phase solvus temperature; and (iii) the precipitation of the hexagonal nitrides and increase in their solvus temperatures.
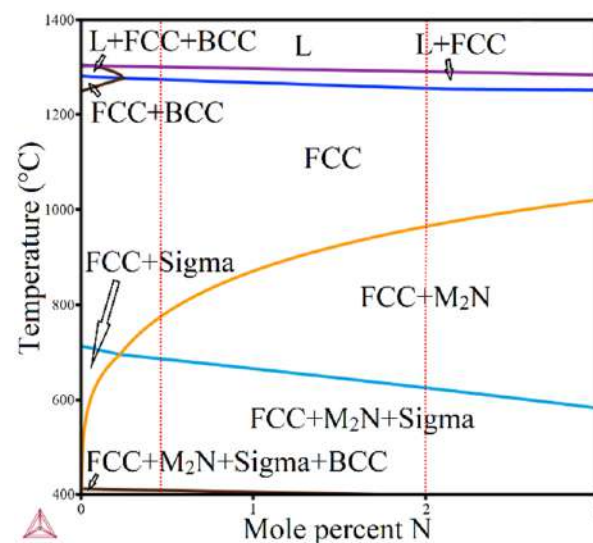

Figure 9. Equilibrium phase diagram produced by ThermoCalc software, showing the effect of nitrogen on the phase composition of the $Fe_{40}Mn_{40}Co_{10}Cr_{10}$ alloy.

The experimental results on the phase composition of the alloys agree well with the CALPHAD prediction. The formation of the σ-phase can be anticipated in the N0 alloy from the phase diagram (Figure 9), but it seems that the predicted solvus temperature of the σ-phase (~700 °C) was significantly underestimated due to the limitations of the available thermodynamic databases [51]. Apparently, the thermodynamic stability of the σ-phase decreases while the stability of the fcc phase increases due to N doping. Thus, no σ-phase was found in the N0.5 alloy in the as-cast state and after annealing at 900 °C. In addition, the precipitation of the M_2N nitrides in the N2 alloy resulted in the partitioning of Cr from the fcc solid solution, further reducing the driving force for the Cr-rich σ-phase formation. Therefore, no σ-particles were found in the N2 alloy even after annealing at 700 °C.

The precipitates can also affect the development of the recrystallization processes in the fcc matrix during the annealing process. For instance, a much lower fcc grain size was found in the N0 and N2 alloys in comparison with the N0.5 alloy after annealing at 700 °C (1.3 vs. 2.4 μm (Table 3)). Finer grains can be associated with either a substantial amount of the coarse σ-particles in the N0 alloy or a smaller amount of the fine nitrides in the N2 alloy due to the well-known Zener drag mechanism [45]. After annealing at 900 °C, all alloys had almost a single fcc phase microstructure with similar grain sizes of 5.6–6.6 μm (Table 3). In addition, the σ-particles tended to precipitate on specific preferred sites, such as prior lamellar boundaries/shear bands, due to the high fcc/σ interphase boundary energy [52]. Thus, a heterogeneous distribution of the σ-particles was obtained, which caused heterogeneity in the fcc grain size (finer grains around the σ-particles, see Figure 4a for example). In turn, N atoms dissolved in the fcc matrix can also affect the recrystallization processes due to the interaction of the interstitial solutes with grain boundaries and the formation of solute atmospheres, thus impeding the migration of grain boundaries and providing a higher energy barrier for recovery and recrystallization during annealing [44,53]. Therefore, only partial recrystallization was observed in the N2 alloy after annealing at 700 °C (Figure 6a).

The mechanical properties of the program alloys varied significantly depending on the N content, processing condition, and testing temperature. Even in the as-cast condition, the alloys demonstrated a strong dependence on the N content (Figure 2). In particular, the strength of the alloys increased in proportion to the N content (except for the N2 alloy at 77 K; this issue will be analyzed in detail). Due to an insignificant amount of the σ-particles in the N0 alloy and coarse grains in the as-cast alloys, which suggest very limited grain boundary strengthening (estimated as ~80 MPa in the N0 alloy and ~35 MPa in the N0.5 and N2 alloys using the Hall–Petch coefficients reported in [8]), the strength increase can mostly be attributed to interstitial solid solution strengthening. Most papers on interstitial fcc HEAs suggest a linear strength increase with increasing dopant content (Ci) [34,38,39]. However, it appears that a more complex dependence was observed in the case of the program alloys. Figure 10 suggests that the strength increase, ΔYS, is proportional to $C_N^{0.5}$, in accordance with the classic Fleisher approach [54]. However, additional, more detailed studies of the solid solution strengthening in the $Fe_{40}Mn_{40}Co_{10}Cr_{10}$-N alloys are required to verify this finding, which is beyond the scope of the current paper. The solid solution strengthening becomes much stronger under cryogenic conditions, in agreement with the previous results [34,35,44].

After thermomechanical processing, well-anticipated tendencies were observed: (i) the alloys became stronger with an increase in the N content, and (ii) an increase in the annealing temperature caused the softening of the alloys, at least at room temperature (Table 4). The microstructure of the alloys became more complicated after processing, and different structural constituents contributed to the strength of the alloys. In addition to interstitial solid solution strengthening, the following strengthening mechanisms are expected to contribute: (i) grain boundary strengthening [41,42]; (ii) precipitation hardening by nitrides [43,44]; (iii) strengthening by the σ-particles in accordance with the rule of the mixture [26]; and (iv) strain (dislocation) hardening due to unrecrystallized areas. Note that significant variations in the structural conditions of the program alloys did

not allow reasonable quantitative analysis. However, it can be assumed that the high strength of the N2 alloy, especially after annealing at 700 °C, may be associated with a combination of interstitial solid solution strengthening, precipitation hardening by nitrides, and work hardening.
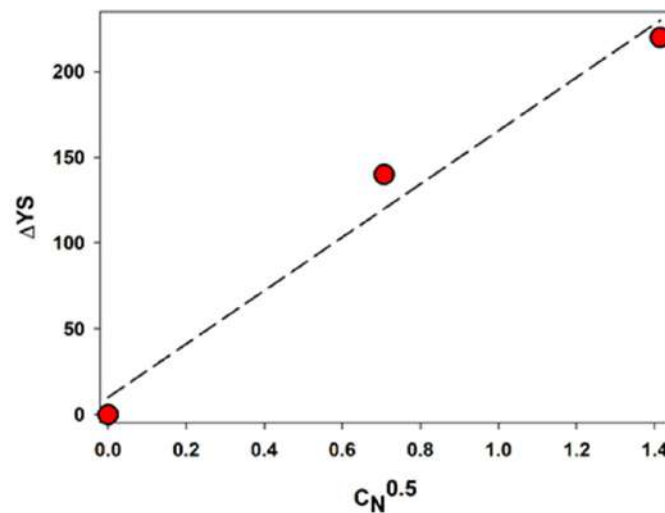

Figure 10. Relationship between the yield strength increase, ΔYS, and N content, C_N, in the program alloys at room temperature. Note that the dashed line is only a guide for eyes.

A decrease in the testing temperature to 77 K resulted in significant strengthening of the program alloys (Tables 2, 4 and 5) under all conditions. According to the previous results [44], the increase in strength can be associated primarily with higher lattice friction and interstitial solid solution hardening. The ductility of the program alloys became lower at cryogenic temperature in comparison to that at cryogenic temperature, which agrees with other reports on the $Fe_{40}Mn_{40}Co_{10}Cr_{10}$-based alloys [55]. Moreover, under some conditions, N0 and N2 alloys demonstrated extreme brittleness at cryogenic temperature.

It seems that there are two main factors that can cause significant embrittlement of the program alloys: (i) the presence of the brittle σ-particles, which can influence both at room and cryogenic temperatures and (ii) the presence of N in the fcc solid solution, influencing the cryogenic temperature. The σ-phase is well-known for its brittleness [30]. The embrittlement of various metallic materials, including steels and HEAs due to the formation of the σ-particles, is well documented [22,25,30,52]. For example, a high amount of σ-particles (32%) likely caused extreme brittleness of the N0 alloy after annealing at 700 °C. However, the effect of the σ-phase should depend on the volume fraction. To verify this assumption, we plotted the dependence of the tensile ductility of the program alloys and several other fcc HEAs contained in the σ-phase (Figure 11). A parabolic-type dependence between the tensile ductility and the σ-phase fraction was observed. From the dependence, one can suggest that (i) the alloys comprising > 30% of the σ-phase were expected to have close to nil tensile ductility; (ii) on the contrary, the alloys with <10% of the σ-particles had high ductility (>40%).

Another reason for the loss in plasticity of the program alloys at 77 K may be the presence of N in the solid solution. A decrease in ductility (and fracture toughness) of N-containing steels [56–59] and fcc HEAs [35,60] at cryogenic temperatures is a well-known phenomenon that is often attributed to the brittle-to-ductile transition. Certain amounts of N can increase the brittle-to-ductile temperature to more than 77 K and thus cause brittle fracture. The data obtained in the current study suggest that in the $Fe_{40}Mn_{40}Co_{10}Cr_{10}$-based alloys, this amount lies in the interval of 0.5–2 at.% of N, as the N0.5 alloy showed adequate ductility at 77 K while the N2 alloy was extremely brittle.
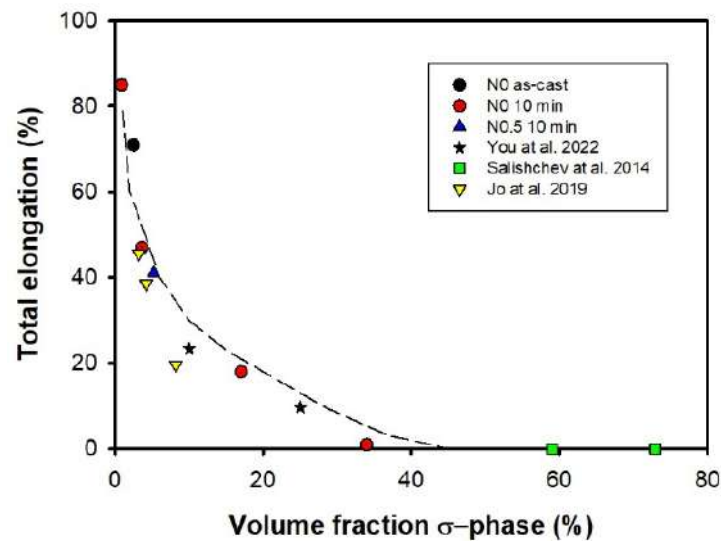
Figure 11. Dependence of tensile ductility on the volume fraction of the σ-phase, data from [22,25,27].

The impact toughness of the program alloys (Table 6) was also often low. The correlation between the impact toughness and tensile ductility of the alloys (Figure 12) suggests that low toughness is associated with the brittleness of the alloys under tension, the reasons of which were described in detail in the previous paragraphs. To ensure adequate toughness ($\geq$25 kJ/m^2), tensile elongation of $\geq$20% is required (see the area separated by the dashed red lines in Figure 12). However, there was no correlation between the toughness values and the tensile properties for the alloys with adequate toughness. Future work is required to find the links between the microstructure, tensile properties, and toughness of the alloy, which is beyond the scope of the current paper.
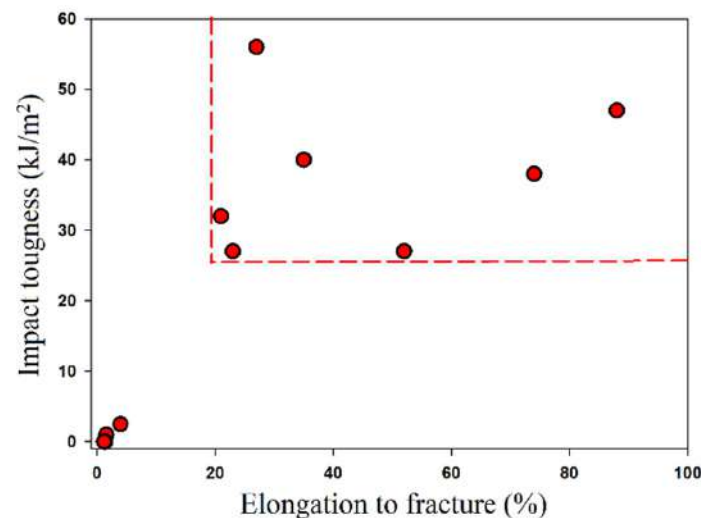

Figure 12. The relationship between the impact toughness and the elongation to fracture of the program alloys.

5. Conclusions

In this study, the structure and mechanical properties of the as-cast and thermomechanicaly processed (cold rolling followed by annealing at 700 °C and 900 °C) $Fe_{40}Mn_{40}Cr_{10}Co_{10}$ (at.%) high-entropy alloys doped with different amounts (0, 0.5, and 2.0 at.%) of N were examined. The following conclusions were drawn:

1. The as-cast $Fe_{40}Mn_{40}Cr_{10}Co_{10}$ alloy (N0) had a dual-phase structure: the σ-phase particles were often found at the boundaries of the coarse fcc grains. The addition of 0.5 (N0.5) and 2.0 (N2) at.% of nitrogen suppressed the formation of the σ-phase and resulted in the coarsening of the fcc grains.

2. The strength of the as-cast alloys at room temperature increased with increasing nitrogen concentration from 160 MPa (N0 alloy) to 380 MPa (N2 alloy). The strength increase was associated with interstitial solid solution strengthening. The alloys also demonstrated good ductility of 54–70%. A decrease in the testing temperature to 77 K resulted in noticeable strengthening and some decrease in ductility of the N0 and N0.5 alloys. The N2 alloy exhibited no ductility at 77 K. The loss in ductility was associated with an increase in the brittle-to-ductile transition temperature due to a high amount of N in the fcc solid solution.

3. Cold rolling of the program alloys resulted in the formation of a lamellar microstructure with a high dislocation density and some shear bands. Annealing after rolling resulted in the development of the static recrystallization and precipitation of additional phases. For example, the σ-phase was found in the N0 alloy after annealing at 700 °C and 900 °C and in the N0.5 alloy after annealing at 700 °C. In turn, hexagonal Cr-rich M_2N nitrides were found in the N2 alloy after annealing at 700 °C. The observed phases agreed reasonably with the CALPHAD data. The precipitation of the σ-phase and the M_2N nitrides in the N0 and N2 alloys, respectively, after annealing at 700 °C resulted in finer fcc grains, presumably due to the pinning effect of the particles.

4. Cold rolling and subsequent annealing resulted in considerable strengthening of the program alloys. The strength of the alloys increased with the N content and decreased with increasing annealing temperature. For example, the N0 alloy after annealing at 700 °C had a yield strength of 650 MPa but low ductility because of a high fraction (32%) of the σ-phase. Meanwhile, the N2 alloy after annealing at 700/900 °C had a yield strength of 900/640 MPa, ultimate tensile strength of 1100/940 MPa, and elongation to fracture of 35/51%. The respective values of Charpy V-notch impact toughness were 23 and 74 kJ/m^2. However, the N2 alloy was brittle at cryogenic temperature due to a high N concentration. The best balance of properties at 77 K was demonstrated by the N0.5 alloy after annealing at 900 °C with a yield strength of 1180 MPa, ultimate tensile strength of 1570 MPa, elongation to fracture of 27%, and impact toughness of 52 kJ/m^2.

References

1. Yeh, J.-W.; Chen, S.K.; Lin, S.-J.; Gan, J.-Y.; Chin, T.-S.; Shun, T.-T.; Tsau, C.-H.; Chang, S.-Y. Nanostructured high-entropy alloys with multiple principal elements: Novel alloy design concepts and outcomes. *Adv. Eng. Mater.* **2004**, *6*, 299–303. [CrossRef]
2. George, E.P.; Raabe, D.; Ritchie, R.O. High-entropy alloys. *Nat. Rev. Mater.* **2019**, *4*, 515–534. [CrossRef]
3. Zhang, Y.; Zuo, T.T.; Tang, Z.; Gao, M.C.; Dahmen, K.A.; Liaw, P.K.; Lu, Z.P. Microstructures and properties of high-entropy alloys. *Prog. Mater. Sci.* **2014**, *61*, 1–93. [CrossRef]
4. Li, W.; Xie, D.; Li, D.; Zhang, Y.; Gao, Y.; Liaw, P.K. Mechanical behavior of high-entropy alloys. *Prog. Mater. Sci.* **2021**, *118*, 100777. [CrossRef]
5. Miracle, D.B.; Tsai, M.-H.; Senkov, O.N.; Soni, V.; Banerjee, R. Refractory high entropy superalloys (RSAs). *Scripta Mater.* **2020**, *187*, 445–452. [CrossRef]
6. Yurchenko, N.; Panina, E.; Roga, Ł.; Shekhawat, L.; Zherebtsov, S.; Stepanov, N. Unique precipitations in a novel refractory Nb-Mo-Ti-Co high-entropy superalloy. *Mater. Res. Let.* **2022**, *10*, 78–87. [CrossRef]
7. Li, Z.; Zhao, S.; Ritchie, R.O.; Meyers, M.A. Mechanical properties of high-entropy alloys with emphasis on face-centered cubic alloys. *Prog. Mater. Sci.* **2019**, *102*, 296–345. [CrossRef]
8. Otto, F.; Dlouhý, A.; Somsen, C.; Bei, H.; Eggeler, G.; George, E.P. The influences of temperature and microstructure on the tensile properties of a CoCrFeMnNi high-entropy alloy. *Acta Mater.* **2013**, *61*, 5743–5755. [CrossRef]
9. Cantor, B.; Chang, I.T.H.; Knight, P.; Vincent, A.J.B. Microstructural development in equiatomic multicomponent alloys. *Mater. Sci. Eng. A* **2004**, *375*, 213–218. [CrossRef]
10. Zhu, C.; Lu, Z.; Nieh, T. Incipient plasticity and dislocation nucleation of FeCoCrNiMn high-entropy alloy. *Acta Mater.* **2013**, *61*, 2993–3001. [CrossRef]
11. Li, Z.; Pradeep, K.G.; Deng, Y.; Raabe, D.; Tasan, C.C. Metastable high-entropy dual-phase alloys overcome the strength-ductility trade-off. *Nature* **2016**, *534*, 227–230. [CrossRef] [PubMed]
12. Kuzminova, Y.; Firsov, D.; Dudin, A.; Sergeev, S.; Zhilyaev, A.; Dyakov, A.; Chupeeva, A.; Alekseev, A.; Martynov, D.; Akhatov, I.; et al. The effect of the parameters of the powder bed fusion process on the microstructure and mechanical properties of CrFeCoNi medium-entropy alloys. *Intermetallics* **2020**, *116*, 106651. [CrossRef]
13. Kuzminova, Y.; Firsov, D.; Dagesyan, S.; Konev, S.; Sergeev, S.; Zhilyaev, A.; Kawasaki, M.; Akhatov, I.; Evlashin, S. Fatigue behavior of additive manufactured CrFeCoNi medium-entropy alloy. *J. Alloy. Compd.* **2021**, *863*, 158609. [CrossRef]
14. Gludovatz, B.; Hohenwarter, A.; Thurston, K.V.S.; Bei, H.; Wu, Z.; George, E.P.; Ritchie, R.O. Exceptional damage-tolerance of a medium-entropy alloy CrCoNi at cryogenic temperatures. *Nat. Commun.* **2016**, *7*, 10602. [CrossRef] [PubMed]
15. Li, Z.; Raabe, D. Strong and Ductile Non-equiatomic High-Entropy Alloys: Design, Processing, Microstructure, and Mechanical Properties. *JOM* **2017**, *69*, 2099–2106. [CrossRef] [PubMed]
16. Povolyaeva, E.; Mironov, S.; Shaysultanov, D.; Stepanov, N.; Zherebtsov, S. Outstanding cryogenic strength-ductility properties of a cold-rolled medium-entropy TRIP Fe$_{65}$(CoNi)$_{25}$Cr$_{9.5}$C$_{0.5}$ alloy. *Mater. Sci. Eng. A* **2022**, *836*, 142720. [CrossRef]
17. Pradeep, K.; Tasan, C.; Yao, M.; Deng, Y.; Springer, H.; Raabe, D. Non-equiatomic high entropy alloys: Approach towards rapid alloy screening and property-oriented design. *Mater. Sci. Eng. A* **2015**, *648*, 183–192. [CrossRef]
18. Deng, Y.; Tasan, C.; Pradeep, K.; Springer, H.; Kostka, A.; Raabe, D. Design of a twinning-induced plasticity high entropy alloy. *Acta Mater.* **2015**, *94*, 124–133. [CrossRef]
19. Rajendrachari, S. An overview of high-entropy alloys prepared by mechanical alloying followed by the characterization of their microstructure and various properties. *Alloys* **2022**, *1*, 116–134. [CrossRef]
20. George, E.P.; Curtin, W.A.; Tasan, C.C. High entropy alloys: A focused review of mechanical properties and deformation mechanisms. *Acta Mater.* **2020**, *188*, 435–474. [CrossRef]
21. Chmielak, L.; Roncery, L.M.; Niederhofer, P.; Weber, S.; Theisen, W. CrMnFeCoNi high entropy alloys with carbon and nitrogen: Mechanical properties, wear and corrosion resistance. *SN Appl. Sci.* **2021**, *3*, 835. [CrossRef]
22. You, D.; Yang, G.; Choa, Y.-H.; Kim, J.-K. Crack-resistant σ/FCC interfaces in the Fe40Mn40Co10Cr10 high entropy alloy with the dispersed σ-phase. *Mater. Sci. Eng. A* **2022**, *831*, 142039. [CrossRef]
23. Li, F.; Sha, Y.; Li, J.; Yang, D.; Zeng, X.; Zhou, X.; Shen, Q.; Liu, M. Influences of recrystallisation and σ phase precipitation on the mechanical properties of CoFeNiMnV high-entropy alloy. *Mater. Tod. Commun.* **2022**, *32*, 103909. [CrossRef]
24. Laplanche, G.; Berglund, S.; Reinhart, C.; Kostka, A.; Fox, F.; George, E. Phase stability and kinetics of σ-phase precipitation in CrMnFeCoNi high-entropy alloys. *Acta Mater.* **2018**, *161*, 338–351. [CrossRef]
25. Salishchev, G.; Tikhonovsky, M.; Shaysultanov, D.; Stepanov, N.; Kuznetsov, A.; Kolodiy, I.; Tortika, A.; Senkov, O. Effect of Mn and V on structure and mechanical properties of high-entropy alloys based on CoCrFeNi system. *J. Alloy. Compd.* **2014**, *591*, 11–21. [CrossRef]
26. Stepanov, N.D.; Shaysultanov, D.G.; Salishchev, G.A.; Tikhonovsky, M.A.; Oleynik, E.E.; Tortika, A.S.; Senkov, O.N. Effect of V content on microstructure and mechanical properties of the CoCrFeMnNiV$_x$ high entropy alloys. *J. Alloy. Compd.* **2015**, *628*, 170–185. [CrossRef]
27. Jo, Y.; Choi, W.; Kim, D.; Zargaran, A.; Lee, K.; Sung, H.; Sohn, S.; Kim, H.; Lee, B.; Lee, S. Utilization of brittle σ phase for strengthening and strain hardening in ductile VCrFeNi high-entropy alloy. *Mater. Sci. Eng. A* **2019**, *743*, 665–674. [CrossRef]
28. Schwind, M.; Källqvist, J.; Nilsson, J.-O.; Ågren, J.; Andrén, H.-O. σ-phase precipitation in stabilized austenitic stainless steels. *Acta Mater.* **2000**, *48*, 2473. [CrossRef]

29. Reed, R.C.; Jackson, M.P.; Na, Y.S. Characterization and modeling of the precipitation of the sigma phase in UDIMET 720 and UDIMET 720LI. *Metall. Mater. Trans. A* **1999**, *30*, 521–533. [CrossRef]
30. Hall, E.O.; Algie, S.H. The sigma phase. *Metall. Rev.* **1966**, *11*, 61–88. [CrossRef]
31. Liu, W.; Lu, Z.; He, J.; Luan, J.; Wang, Z.; Liu, B.; Liu, Y.; Chen, M.; Liu, C. Ductile CoCrFeNiMo$_x$ high entropy alloys strengthened by hard intermetallic phases. *Acta Mater.* **2016**, *116*, 332–342. [CrossRef]
32. Laplanche, G.; Volkert, U.F.; Eggeler, G.; George, E.P. Oxidation behavior of the CrMnFeCoNi high-entropy alloy. *Oxid. Met.* **2016**, *85*, 629. [CrossRef]
33. Varvenne, C.; Luque, A.; Curtin, W.A. Theory of strengthening in fcc high entropy alloys. *Acta Mater.* **2016**, *118*, 164. [CrossRef]
34. Klimova, M.V.; Semenyuk, A.O.; Shaysultanov, D.G.; Salishchev, G.A.; Zherebtsov, S.V.; Stepanov, N.D. Effect of carbon on cryogenic tensile behavior of CoCrFeMnNi-type high entropy alloys. *J. Alloy. Compd.* **2019**, *811*, 152000. [CrossRef]
35. Klimova, M.; Shaysultanov, D.; Semenyuk, A.; Zherebtsov, S.; Salishchev, G.; Stepanov, N. Effect of nitrogen on mechanical properties of CoCrFeMnNi high entropy alloy at room and cryogenic temperatures. *J. Alloy. Compd.* **2020**, *849*, 156633. [CrossRef]
36. Wu, Z.; Parish, C.; Bei, H. Nano-twin mediated plasticity in carbon-containing FeNiCoCrMn high entropy alloys. *J. Alloy. Compd.* **2015**, *647*, 815–822. [CrossRef]
37. Han, Y.; Li, H.B.; Feng, H.; Li, K.M.; Tian, Y.Z.; Jiang, Z.H. Enhancing the strength and ductility of CoCrFeMnNi high-entropy alloy by nitrogen addition. *Mat. Sci. Eng. A* **2020**, *789*, 139587. [CrossRef]
38. Wang, Z.W.; Baker, I.; Guo, W.; Poplawsky, J.D. The effect of carbon on the microstructures, mechanical properties, and deformation mechanisms of thermo-mechanically treated Fe$_{40.4}$Ni$_{11.3}$Mn$_{34.8}$Al$_{7.5}$Cr$_6$ high entropy alloys. *Acta Mater.* **2017**, *126*, 346–360. [CrossRef]
39. Wang, Z.W.; Bei, H.B.; Baker, I. Microband induced plasticity and the temperature dependence of the mechanical properties of a carbon-doped FeNiMnAlCr high entropy alloy. *Mater. Charact.* **2018**, *139*, 373–381. [CrossRef]
40. Egilmez, M.; Abuzaid, W. Magnetic, electrical and mechanical properties of Fe$_{40}$Mn$_{40}$Co$_{10}$Cr$_{10}$. *Scient. Rep.* **2021**, *11*, 1–12. [CrossRef]
41. Xiong, F.; Fu, R.D.; Li, Y.J.; Xu, B.W.; Qi, X.W. Influences of nitrogen alloying on microstructural evolution and tensile properties of CoCrFeMnNi high-entropy alloy treated by cold-rolling and subsequent annealing. *Mat. Sci. Eng. A* **2020**, *787*, 139472. [CrossRef]
42. Liu, X.W.; Gao, N.; Zheng, J.; Wu, Y.; Zhao, Y.Y.; Chen, Q.; Zhou, W.; Pu, S.Z.; Jiang, W.M.; Fan, Z.T. Improving high-temperature mechanical properties of cast CrFeCoNi high-entropy alloy by highly thermostable in-situ precipitated carbides. *J. Mater. Sci. Technol.* **2020**, *72*, 29–38. [CrossRef]
43. Xiong, F.; Fu, R.-D.; Li, Y.-J.; Sang, D.-L. Effects of nitrogen alloying and friction stir processing on the microstructures and mechanical properties of CoCrFeMnNi high-entropy alloys. *J. Alloy. Compd.* **2020**, *822*, 153512. [CrossRef]
44. Semenyuk, A.; Klimova, M.; Shaysultanov, D.; Salishchev, G.; Zherebtsov, S.; Stepanov, N. Effect of nitrogen on microstructure and mechanical properties of the CoCrFeMnNi high-entropy alloy after cold rolling and subsequent annealing. *J. Alloy. Compd.* **2021**, *888*, 161452. [CrossRef]
45. He, M.Y.; Shen, Y.F.; Jia, N.; Liaw, P.K. C and N doping in high-entropy alloys: A pathway to achieve desired strength-ductility synergy. *Mater. Today* **2021**, *25*, 101162. [CrossRef]
46. Seol, J.B.; Bae, J.W.; Li, Z.; Han, J.C.; Kim, J.G.; Raabe, D.; Kim, H.S. Boron doped ultrastrong and ductile high-entropy alloys. *Acta Mater.* **2018**, *151*, 366–376. [CrossRef]
47. Shima, S.H.; Moon, J.; Pouraliakbar, H.; Lee, B.J.; Hong, S.I.; Kim, H.S. Toward excellent tensile properties of nitrogen-doped CoCrFeMnNi high-entropy alloy at room and cryogenic temperatures. *J. Alloy. Compd.* **2022**, *897*, 163217. [CrossRef]
48. Moravcik, I.; Cizek, J.; Gouvea, L.; Cupera, J.; Guban, I.; Dlouhy, I. Nitrogen Interstitial Alloying of CoCrFeMnNi High Entropy Alloy through Reactive Powder Milling. *Entropy* **2019**, *21*, 363. [CrossRef] [PubMed]
49. Han, Y.; Li, H.; Feng, H.; Tian, Y.; Jiang, Z.; He, T. Mechanism of dislocation evolution during plastic deformation of nitrogen-doped CoCrFeMnNi high-entropy alloy. *Mater. Sci. Eng. A* **2021**, *814*, 141235. [CrossRef]
50. Astafurova, E.G.; Melnikov, E.V.; Reunova, K.A.; Moskvina, V.A.; Astafurov, S.V.; Panchenko, M.Y.; Mikhno, A.S.; Tumbusova, I. Temperature Dependence of Mechanical Properties and Plastic Flow Behavior of Cast Multicomponent Alloys Fe$_{20}$Cr$_{20}$Mn$_{20}$Ni$_{20}$Co$_{20-x}$C$_x$ (x = 0, 1, 3, 5). *Phys. Mesomech.* **2021**, *24*, 674–683. [CrossRef]
51. Klimova, M.; Stepanov, N.; Shaysultanov, D.; Chernichenko, R.; Yurchenko, N.; Sanin, V.; Zherebtsov, S. Microstructure and mechanical properties evolution of the Al, C-containing CoCrFeNiMn-type high-entropy alloy during cold rolling. *Materials* **2018**, *11*, 53. [CrossRef] [PubMed]
52. Senkov, O.N.; Miracle, D.B.; Chaput, K.J.; Couzinie, J.-P. Development and exploration of refractory high entropy alloys-A. review. *J. Mater. Res.* **2018**, *33*, 1–37. [CrossRef]
53. Hsieh, C.-C.; Wu, W. Overview of Intermetallic Sigma (σ) Phase Precipitation in Stainless Steels. *Internat. Schol. Res. Netw.* **2012**, *2012*, 1–16. [CrossRef]
54. Humphreys, F.J.; Hatherly, M. *Recrystallization and Related Annealing Phenomena*; Elsevier Science Ltd: Oxford, UK, 1995.
55. Fleischer, R.L. Substitutional solution hardening Durcissement de solution par substitution Verfestigung in substitutionsmischkkistallen. *Acta Metall. Sin.* **1963**, *11*, 203–209. [CrossRef]
56. Tang, K.; Wu, Y.K.; Wei, R.; Chen, L.B.; Lu, S.; Qi, Y.L.; Jiang, F.; Sun, J. Achieving superior cryogenic tensile properties in a Ti-doped (Fe$_{40}$Mn$_{40}$Co$_{10}$Cr$_{10}$)$_{96.7}$C$_{3.3}$ high-entropy alloy by recovering deformation twinning. *Mat. Sci. Eng. A* **2021**, *808*, 140927. [CrossRef]

57. Vogt, J.-B.; Messai, A.; Foct, J. Cleavage fracture of austenite induced by nitrogen supersaturation. *Scripta Metallur. Mater.* **1994**, *31*, 549–554. [CrossRef]
58. Müllner, P.; Solenthaler, C.; Uggowitzer, P.J.; Speidel, M.O. Brittle fracture in austenitic steel. *Acta Metallur. Mater.* **1994**, *42*, 2211–2217. [CrossRef]
59. Tomota, Y.; Xia, Y.; Inoue, K. Mechanism of low temperature brittle fracture in high nitrogen bearing austenitic steels. *Acta Mater.* **1998**, *46*, 1577–1587. [CrossRef]
60. He, Z.F.; Jia, N.; Wang, H.W.; Yan, H.L.; Shen, Y.F. Synergy effect of multi-strengthening mechanisms in FeMnCoCrN HEA at cryogenic temperature. *J. Mater. Sci. Technol.* **2021**, *86*, 158–170. [CrossRef]